Dalton Transactions

PAPER

View Article Online
View Journal | View Issue

Cite this: *Dalton Trans.*, 2018, **47**, 4105

Mismatch in cation size causes rapid anion dynamics in solid electrolytes: the role of the Arrhenius pre-factor†

Stefan Breuer *[a] and Martin Wilkening [a,b]

Crystalline ion conductors exhibiting fast ion dynamics are of utmost importance for the development of, *e.g.*, sensors or rechargeable batteries. In some layer-structured or nanostructured compounds fluorine ions participate in remarkably fast self-diffusion processes. As has been shown earlier, F ion dynamics in nanocrystalline, defect-rich BaF_2 is much higher than that in the coarse-grained counterpart BaF_2. The thermally metastable fluoride $(Ba,Ca)F_2$, which can be prepared by joint high-energy ball milling of the binary fluorides, exhibits even better ion transport properties. While long-range ion dynamics has been studied recently, less information is known about local ion hopping processes to which ^{19}F nuclear magnetic resonance (NMR) spin–lattice relaxation is sensitive. The present paper aims at understanding ion dynamics in metastable, nanocrystalline $(Ba,Ca)F_2$ by correlating short-range ion hopping with long-range transport properties. Variable-temperature NMR line shapes clearly indicate fast and slow F spin reservoirs. Surprisingly, from an atomic-scale point of view increased ion dynamics at intermediate values of composition is reflected by increased absolute spin–lattice relaxation rates rather than by a distinct minimum in activation energy. Hence, the pre-factor of the underlying Arrhenius relation, which is determined by the number of mobile spins, the attempt frequency and entropy effects, is identified as the parameter that directly enhances short-range ion dynamics in metastable $(Ba,Ca)F_2$. Concerted ion migration could also play an important role to explain the anomalies seen in NMR spin–lattice relaxation.

Received 28th November 2017,
Accepted 10th February 2018

DOI: 10.1039/c7dt04487a

rsc.li/dalton

Introduction

The irregular movement of small anions and cations in crystalline and amorphous solids is a natural phenomenon that plays a key role in many devices as well as technological and geological processes. Extracting general rules from the existing amount of experimental data that control ionic transport and ionic diffusivity is, thus, of importance if we want to optimize devices, such as batteries,[1–4] relying on dynamic processes of ions. Nanostructured materials play a prominent role in these fields.[1,5,6]

Although ion dynamics in a huge number of various nanomaterials have been studied over the last decades with a wide range of techniques,[7–11] our picture about ionic diffusivity is far from being completely understood. The introduction of defects, that is, in a more general sense describable with structural disorder, represents a powerful instrument with which we can control the chemical and physical properties of a material.[12–17] Ion dynamics sensitively depend on local arrangements. The present work is aimed at describing the interrelations between local disorder and short-range ion dynamics using a suitable model substance that may also be of interest as a fast ion conducting solid electrolyte.[4,18–23]

The metastable (quasi) solid-solution $(Ba,Ca)F_2$ served as such model substance.[24,25] Recently, it has also attracted groups from theory to model ion conductivities.[26,27] Nanocrystalline $Ba_{1-x}Ca_xF_2$ ($0 < x < 1$) can easily be prepared by mechanochemical reaction at low temperatures from the binary fluorides BaF_2 and CaF_2.[24,25] Joint milling the two fluorides forces the cations to mix at atomic scale while the symmetry of the educts remains the same; both BaF_2 and CaF_2 crystallize with antifluorite structure. Thus, over the entire compositional range the original crystal symmetry is preserved whereas local atomic arrangements do, however, differ.[28] At $x = 0.5$, and after sufficiently long mechanical treatment, the majority of the F anions are directly surrounded by both Ba and Ca ions without any heavy clustering of Ba- and Ca-rich regions.[28] These features, as well as the possibility to prepare incompletely mixed samples, render $Ba_{1-x}Ca_xF_2$ a complex

[a]*Christian Doppler Laboratory for Lithium Batteries and Institute for Chemistry and Technology of Materials, Graz University of Technology (NAWI Graz), Stremayrgasse 9, 8010 Graz, Austria*
[b]*ALISTORE-ERI European Research Institute, 33 rue Saint Leu, 80039 Amiens, France*
† Electronic supplementary information (ESI) available: XRPD patterns, crystallite sizes, deconvoluted ^{19}F MAS NMR spectra. See DOI: 10.1039/c7dt04487a

model system to study the influence of structural disorder on local ion dynamics.

Although the mixing effect on (i) atomic structure and (ii) long-range ion transport in $Ba_{1-x}Ca_xF_2$ has recently been studied *via* DC conductivity measurements in detail,[28] less is known about the change of local hopping processes. Starting from $x = 0$ the ionic conductivity increases and passes through a maximum at approximately $x = 0.5$ before it decreases and reaches the value of pure CaF_2 ($x = 1$).[28] In turn, the associated activation energy runs through a minimum at $x = 0.5$ being the composition with maximum structural disorder with regard to intimate cation mixing. The specific conductivity of the solid solution $Ba_{0.5}Ca_{0.5}F_2$ prepared by ball milling exceeds even that of epitaxially grown BaF_2–CaF_2–BaF_2 layers.[28,29] This layered system[29] is one of the most famous examples of an artificial ion conductor whose transport properties are explained by non-trivial size effects, *i.e.*, by overlapping space charge zones.[9,10,30,31] Such effects might also influence ion transport in mechanosynthesized $(Ba,Ca)F_2$.[28]

While local strain, *i.e.*, a strongly heterogeneous potential landscape, has been made responsible for the increase in conductivity of $Ba_{0.5}Ca_{0.5}F_2$,[28] short-range ion dynamics have so far not been probed. Shedding light on these hopping processes is expected to help identify the driving forces that control the increase in ionic diffusivity seen. Here, we took advantage of ^{19}F NMR (spin-lock) relaxometry to extract mean activation barriers the ions are subjected to in $Ba_{1-x}Ca_xF_2$. For heterogeneous nanocrystalline materials with disordered interfacial regions and crystalline grains NMR can, in ideal cases, differentiate the mobile ions in or near the (percolating) interfaces from those in the defect-rich interior of the nm-sized grains.[32–34] For Li_2O and the dispersed, nanocrystalline ion conductors $Li_2O : X_2O_3$ (X = Al, B) it was possible to draw conclusions about the location of the mobile ions responsible for fast macroscopic ion transport.[32,33]

Experimental

Mechanochemical preparation and characterization of the samples

A series of nanocrystalline samples $Ba_{1-x}Ca_xF_2$ with the compositions of $x = 0$, 0.1, 0.2, 0.5, 0.8, 1.0 were prepared by high-energy ball milling. Pure, microcrystalline BaF_2 (99.99%, Sigma-Aldrich) and CaF_2 (99.9%, ABCR) served as starting materials. We used of a Fritsch Pulverisette 7 (premium line) planetary mill. Two 45 mL grinding beakers, filled with the reactants (the total mass was 4 g) and 180 ZrO_2 milling balls (5 mm in diameter) in each case, were employed. The mixtures were mechanically treated for 10 h at a rotational speed of 600 rpm. To exclude contamination with moisture or oxygen during milling, the beakers were filled and emptied in a glovebox with dry argon atmosphere. The powders obtained were characterized by X-ray powder diffraction (XRPD) using a Bruker D8 Advance diffractometer that operates with Bragg Brentano geometry and Cu K_α radiation.

Conductivity measurements

For our conductivity measurements cylindrical pellets with 5 mm in diameter and *ca.* 1.5 mm in thickness were used. The pellets were uniaxially cold-pressed at a pressure of approximately 0.5 GPa. Blocking electrodes with a layer thickness of 100 nm were applied with a Leica EM SCD 050 evaporator. Impedance measurements were carried out with a Novocontrol Concept 80 broadband dielectric spectrometer. Our measurements covered a frequency range from 0.01 Hz to 10 MHz; temperatures (173 K–473 K) were adjusted with a QUATRO controller (Novocontrol). To avoid any contamination with water or oxygen during the measurements, the pellets were dried inside the impedance cell, which was permanently flushed with dry nitrogen gas.

NMR measurements

To assess the fluorine self-diffusion parameters ^{19}F NMR spectroscopy and relaxometry were used to estimate jump rates and activation energies. Here, we took advantage of the saturation recovery and the spin-lock technique to record longitudinal ($1/T_1$) as well as transversal ($1/T_{1\rho}$) NMR spin–lattice relaxation (SLR) rates. For the NMR measurements the dry powders were fire-sealed in Duran glass tubes (*ca.* 4 cm in length and 3 mm in diameter) under vacuum to protect them from any impact of humidity. All measurements were carried out on a Bruker Avance III spectrometer that was connected to a shimmed cryomagnet with a nominal magnetic field of 7 T. This field corresponds to a ^{19}F NMR Larmor frequency of $\omega_0/2\pi = 282.0$ MHz. A home-built NMR probe, which is suitable to record NMR signals under static conditions in a temperature range from 193 K to 533 K, was used to record the SLR rates and the ^{19}F NMR spectra. At 200 W the $\pi/2$ pulse length was approximately 1 μs. A Eurotherm temperature controller in combination with a type-T thermocouple was utilized for both temperature controlling and monitoring. The saturation recovery pulse sequence consisted of ten succeeding pulses that destroy any longitudinal magnetization M_z, after a delay time t_d the reading pulse was sent to detect the recovery of M_z as a free induction decay (FID): $10 \times \pi/2$-$t_d - \pi/2$-acquisition (acq.). To construct the magnetization transients $M_z(t_d)$ we plotted the area under the FIDs *vs.* t_d. Additionally, rotating-frame ^{19}F NMR SLRρ rates $1/T_{1\rho}$ were measured by means of the spin-lock technique, $\pi/2$ $p(t_{lock})$-acq., using a locking frequency $\omega_1/2\pi$ of approximately 100 kHz.[18,35] We varied the locking pulse length from $t_{lock} = 46$ μs to $t_{lock} = 460$ ms. To guarantee full longitudinal relaxation between each scan the recycle delay was set to at least $5 \times T_1$. Both the $1/T_1$ and $1/T_{1\rho}$ rates were obtained by parameterizing the resulting transients $M_z(t_d)$ and $M_\rho(t_{lock})$ with stretched exponentials of the form $M_z(t_d) \propto 1 - \exp(-(t_w/T_1)^\gamma)$ and $M_\rho(t_{lock}) \propto \exp(-(t_{lock}/T_{1\rho})^\kappa)$, respectively. While the stretching exponents γ varied from 1 to 0.8, the parameter κ ranged from 0.4 to 1.0 depending on temperature.

Static ^{19}F NMR spectra were obtained with a single 90° pulse experiment *via* Fourier transformation of the FID. We employed a 500 MHz Avance spectrometer (Bruker) to record

the spectra; the ^{19}F Larmor frequency was 470.4 MHz. The NMR lines shown represent Fourier transforms recorded under static, *i.e.*, non-rotating, conditions. ^{19}F NMR spectra under magic angle spinning (MAS) were measured at a rotation speed of 60 kHz using 1.3 mm rotors. Spectra were referenced to crystalline CaF_2, which shows, as a secondary reference, an isotropic chemical shift δ_{iso} of 58 ppm; C_6F_6 served as primary reference.

Results and discussion

Characterization *via* X-ray powder diffraction and ^{19}F MAS NMR

The phase purity of the samples and the formation of a mixed $(Ba,Ca)F_2$ phase with retained cubic symmetry (see Fig. 1) was verified with the help of XRPD. We collected diffraction patterns at room temperature and in air atmosphere. Exemplarily, Fig. 1(a) shows the pattern of the mixture with the composition $Ba_{0.2}Ca_{0.8}F_2$ which was milled for 10 h in the P7 planetary mill (see Fig. S1 in the ESI† for the characterization of the other samples studied). For comparison, in Fig. 1 the patterns of nanocrystalline BaF_2 and CaF_2 prepared under the same milling conditions are presented. The pure nanocrystalline samples feature reflections at exactly the same positions as their coarse-grained samples. A marked difference is, however, that the reflections of the powders ball-milled for 10 h show noticeable broadening. This broadening is attributed to the formation of nm-sized crystallites and the generation of strain upon mechanical treatment. As has been shown by earlier studies on nanocrystalline $(Ba,Ca)F_2$ as well as other fluorides and oxides prepared by high-energy ball milling the final average crystallite size reached after many hours of mechanical treatment is in the order of 10 to 17 nm for the mixed samples.[36] This result was obtained by evaluating the width of the reflections with the equation introduced by Scherrer[37] (see ESI (Table S1†) for the exact crystallite sizes calculated). These values are supported by high-resolution transmission electron microscopy carried out in early studies.[24,25] It is worth noting that abrasion of ZrO_2 on ion conductivities turned out to be negligible in our case; such effects have been discussed by some of us in earlier studies.[24,25,28]

A close look at the pattern of the $Ba_{0.2}Ca_{0.8}F_2$ mixture reveals that the reflections shifted to smaller diffraction angles if compared with those of pure (nanocrystalline) CaF_2. The incorporation of the larger Ba^{2+} ions (ionic radius of 1.42) into the F-sublattice of CaF_2, the ionic radius of Ca^{2+} is 1.12, causes the original lattice to expand. According to Bragg's law this mismatch in size results in lower diffraction angles. The reverse process is observed when some Ca^{2+} ions are introduced into BaF_2. For $Ba_{1-x}Ca_xF_2$ with x = 0.5 the final reflections are characterized by almost the arithmetic average.[28] The

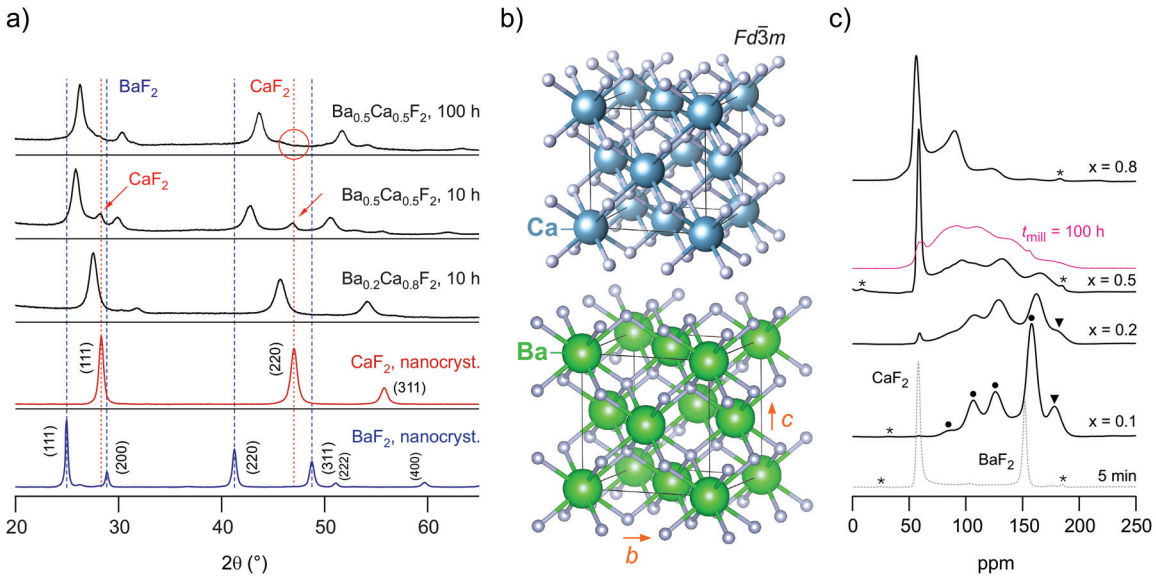

Fig. 1 (a) X-ray powder patterns of high-energy ball milled CaF_2, BaF_2 and a mixtures $Ba_{1-x}Ca_xF_2$ with the compositions $Ba_{0.2}Ca_{0.8}F_2$ and $Ba_{0.5}Ca_{0.5}F_2$. From the point of view of XRPD, the pattern of the mixed phase with x = 0.8 reveals the formation of a nanocrystalline solid solution as all reflections refer to a cubic phase with shifts to lower diffraction angles. The same holds for x = 0.2. The samples were prepared in a planetary mill using a ZrO_2 vial set; the rotational speed was 600 rpm, the milling time was set to 10 h. To prepare $Ba_{0.5}Ca_{0.5}F_2$ free of any residuals of nanocrystalline $Ca(Ba)F_2$ longer milling times are needed. The conductivity response of the two samples is the same. (b) Crystal structure of cubic CaF_2 and BaF_2; the two materials only differ by the lattice constant a. (c) ^{19}F MAS NMR spectra of $Ba_{1-x}Ca_xF_2$ recorded at 470.4 MHz and a spinning frequency of 60 kHz. The asterisks mark spinning sidebands, the black dots (x = 0.1) indicate the different F environments. Note that signals arising from orthorhombic BaF_2, as also seen in X-ray diffraction (see Fig. 1(a)), are marked by red dots; these partly overlap with those from the mixed phases. If not stated otherwise, the milling time was 10 h. The spectrum, referring to a milling time of 5 min, shows a stochiometric mixture of BaF_2 and CaF_2 to highlight the initial δ_{iso} values of the starting materials, 58 ppm (CaF_2) and 152 ppm (BaF_2), respectively.

formation of mixed $(Ba,Ca)F_2$ and the discussion of the corresponding XRPD patterns is already well documented in literature.[24,25,28] Most important for us is the following aspect: after milling the educts for 10 h, the reflections originating from the non-mixed starting materials BaF_2 are no longer visible for most compositions. As an example, for $Ba_{0.2}Ca_{0.8}F_2$ the formation of a mixed phase with no significant amounts of crystalline educts is seen by XRPD.

Besides decreasing the crystallite size and introducing structural disorder, it cannot be ruled out that mechanical treatment also lead to the formation of some amorphous material. Although recent EXAFS studies by Chadwick and coworkers[38] did not point to large fractions of amorphous regions in mechanosynthesized $Ba_{1-x}Ca_xF_2$, the XRPD pattern of $Ba_{0.2}Ca_{0.8}F_2$ revealed a shallow hump at low diffraction angles. This feature is frequently assigned to amorphous material.[39]

For samples with x being close to 0.5, *i.e.*, considering equimolar mixtures, longer milling times than 10 h are needed to ensure intimate mixing of the earth alkaline cations. As an example, in Fig. 1 the XRPD pattern of two samples of $Ba_{0.5}Ca_{0.5}F_2$ are shown that were obtained after milling for t_{mill} = 10 h and 100 h, respectively. After 10 h residual CaF_2 is still present and not all Ca^{2+} ions have been fully incorporated into the BaF_2 lattice, as can be seen by the small CaF_2 reflections visible (see the red arrows in Fig. 1(a)). After milling the mixture for 100 h these reflections disappear. Additionally, the more Ca^{2+} ions are introduced into the BaF_2 lattice the larger the lattice contraction of BaF_2 which in turn causes a shift of the reflections toward larger diffraction angles. Hence, only very long milling times ensured the absence of any (nanocrystalline) starting materials.

The positions of the final reflections of the sample obtained after 100 h suggest the formation of an almost fully mixed sample. Of course, the existence of both Ba-rich and Ca-rich regions cannot be excluded on the basis of XRPD. As seen by (high-resolution) ^{19}F MAS NMR, which is sensitive to the local, atomic environments of the F nuclei, heavy clustering, however, seems to be negligible for x = 0.5. This conclusion is at least valid for mixtures obtained after sufficiently long periods of milling with t_{mill} = 100 h (see Fig. 1c). The ^{19}F MAS NMR spectra of the fully mixed samples are composed of several overlapping lines revealing partly the magnetically inequivalent F anions in $Ba_{0.5}Ca_{0.5}F_2$. In general, since each F anion is directly surrounded by 4 cations, in an ideal solid solution the environments are $[Ba]_3[Ca]$, $[Ba]_2[Ca]_2$, $[Ba][Ca]_3$ as well as $[Ba]_4$ and $[Ca]_4$ (see Fig. S2 in the ESI† for the assignment of the different atomic F environments in Ba-rich $Ba_{1-x}Ca_xF_2$ including a deconvolution of the spectra).[28]

The signals of $[Ba]_4$ and $[Ca]_4$ are the weakest in intensity for x = 0.5 and t_{mill} = 100 h. Keeping in mind that the NMR chemical shift for $[Ba]_4$ in completely mixed $Ba_{0.5}Ca_{0.5}F_2$ (182 ppm) is different compared to that in pure nanocrystalline BaF_2 (152 ppm), the NMR spectra point to mixing of the earth alkaline ions on atomic scale. For the sample milled only for 10 h (x = 0.5) we see that the sharp signal around 52 ppm points to Ca-rich regions that only vanish if t_{mill} is increased to 100 h. The reason for the disappearance of the $[Ca]_4$ signal is, that more and more CaF_2 gets incorporated into BaF_2 the longer the milling time is chosen. After 100 h of milling, the equimolar mixture forms a disordered phase with a large amount of mixed F environments: $[Ba]_3[Ca]$, $[Ba]_2[Ca]_2$, $[Ba][Ca]_3$. The more effective the mixing process is, the less the probability to find Ba- and Ca-rich species $[Ba]_4$ and $[Ca]_4$ originating from the educts (see also the corresponding XRPD pattern in Fig. 1(a)).

When comparing the samples with x = 0.8 and x = 0.1 it is, however, evident that after a milling period of 10 h Ca-rich and Ba-rich regions are clearly present. The Ca-rich sample (x = 0.8) reveals the fastest ^{19}F SLR rates, see below. ^{19}F MAS NMR reveals further that mixing of the earth-alkaline ions seems to be easier for compositions x < 0.5, *i.e.*, for Ba-rich samples. Mechanical treatment of cubic-BaF_2 always leads to the formation of some orthorhombic material (up to 20 wt% depending on the milling conditions). The orthorhombic form is a high-pressure phase of BaF_2; it is also seen in ^{19}F MAS NMR. With increasing x the amount of orthorhombic BaF_2 decreases.

As outlined above, after the formation of the mixed phase, either completely or partially, the F anion conductivity σ_{DC} sharply increases when compared to the pure nanocrystalline starting materials. σ_{DC} passes through a maximum at intermediate compositions. Correspondingly, the activation energy takes a minimum at x = 0.5. While σ_{DC} refers to long-range ion transport, that is affected by grain boundaries, interfacial regions and porosity, NMR relaxometry, on the other hand, is primarily sensitive to bulk properties and, most importantly, to local F^- hopping processes. In ideal cases, NMR was able to differentiate between ions in the interfacial regions and those in the bulk. This separation was possible for some single- and two-phase nanocrystalline oxides as well as binary fluorides with a large number fraction of ions residing in the structurally disordered interfacial regions.

^{19}F NMR relaxometry to evaluate short-range F anion hopping

In Fig. 2 an overview of all variable-temperature ^{19}F spin–lattice and spin-lock NMR relaxation rates is presented. To identify the thermally activated regions, from which hopping activation energies can be extracted, the rates were plotted in an Arrhenius representation. Stretched exponential functions served to parameterize the magnetization transients $M_z(t_d)$ and $M_\rho(t_{lock})$, see Fig. 3(a) and (b) and section 2. The corresponding stretching exponents γ are illustrated in Fig. 3(c).

The stretching factors of the $M_z(t_d)$ transients, which contain the rate T_1, are almost exponential, except for few compositions deviations from γ = 1 show up at temperatures above 393 K. The κ values of the spin-lock transients reveal a more complex behavior and pass through minima at temperatures higher than 333 K; this feature is especially seen for the mixed sample $Ba_{0.5}Ca_{0.5}F_2$. The educts, which are characterized by lower ionic conductivities (see below), do not show such behav-

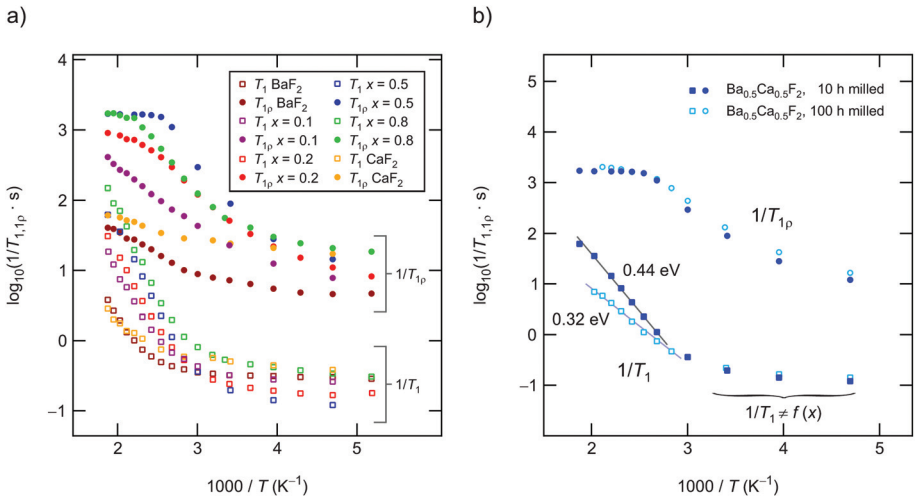

Fig. 2 (a) Temperature dependence of the ^{19}F NMR SLR rates $1/T_1$ (282.0 MHz) and $1/T_{1\rho}$ (100 kHz) for all nanocrystalline samples $Ba_{1-x}Ca_xF_2$ prepared *via* high-energy ball milling. (b) ^{19}F NMR SLR behavior of nanocrystalline $Ba_{0.5}Ca_{0.5}F_2$ obtained after t_{mill} = 10 h and t_{mill} = 100 h. While measurements in the kHz range ($1/T_{1\rho}$) are unaffected by t_{mill}, local jump processes, as seen by T_1 NMR, depend on the degree of cation mixing. The activation energies indicated refer to non-corrected rates; background correction to calculate $1/T_{1diff}$ changes E_a from 0.32 eV to 0.35 eV (100 h) and from 0.44 eV to 0.49 eV with no effect on the ratio of the two activation energies.

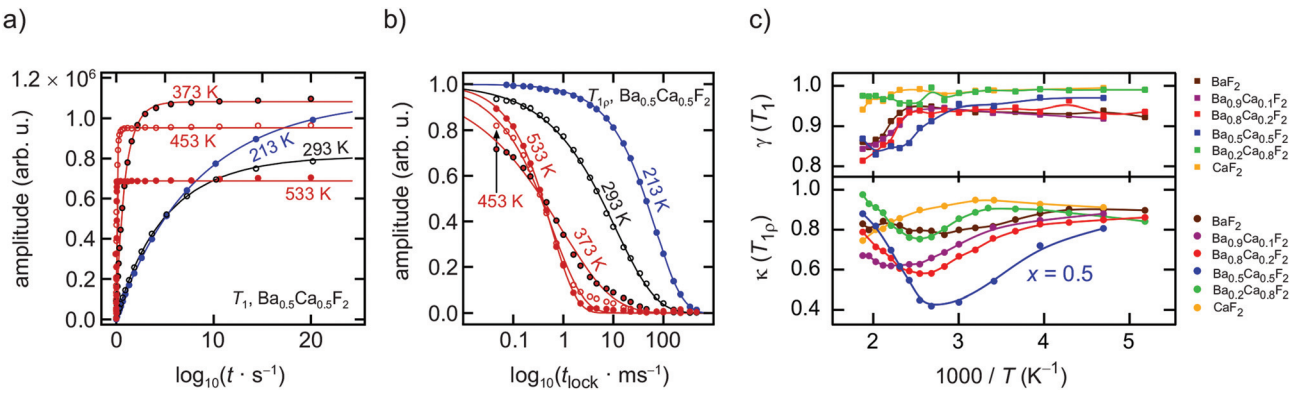

Fig. 3 (a) Selected variable-temperature ^{19}F NMR T_1 transients of nanocrystalline $Ba_{0.5}Ca_{0.5}F_2$. The solid lines represent fits according to stretched exponentials: $M_z(t_d) \propto 1 - \exp(-(t/T_1)^{\gamma})$. (b) Spin-lock ^{19}F NMR $T_{1\rho}$ magnetization transients of the same sample shown in (a); the amplitude was scaled such that it ranges from 0 to 1. The solid lines represent fits according to M_ρ (t_{lock}) $\propto \exp(-(t_{lock}/T_{1\rho})^{\kappa})$. (c) Change of γ and κ as a function of the inverse temperature $1/T$.

ior. The $Ba_{0.5}Ca_{0.5}F_2$ sample features the lowest minimum with values of approximately $\kappa = 0.4$ at $T = 360$ K.

For all samples the ^{19}F NMR SLR rates, measured in the laboratory frame of reference ($1/T_1$), show a non-diffusion induced regime below 330 K. In this T range the rates only marginally depend on temperature, see also Fig. 4(a). Background relaxation is in many cases driven by lattice vibrations or coupling of the spins to paramagnetic impurities.[40]

Above 330 K the rates start to increase because of F jumps on the time scale of the NMR experiment. We approximated the background rates with a power law, $1/T_{1,bgr} \propto T^{\beta}$, and extrapolated the rates to higher T to calculate background-free, diffusion-induced rates: $1/T_{1diff} = 1/T_1 - 1/T_{1,bgr}$.[41] β values ranged from 0.3 ($x = 0$) to 1.5 ($x = 0.5$). For intermediate values of x we obtained $\beta \approx 1$. In Fig. 4(a) this procedure is exemplarily shown for nanocrystalline BaF_2, see unfilled symbols. The rates $1/T_{1diff}$ follow Arrhenius behavior characterized by an activation energy of 0.4 eV.

As x in $Ba_{x-1}Ca_xF_2$ is increased, the beginning of the diffusion-induced flank is shifted toward lower T. This clearly indicates increased F self-diffusion in the partially or completely mixed phases. As can be already seen in Fig. 4(a), the slope of the different flanks do not vary much but run in parallel to each other. The diffusion induced rates, see Fig. 4(b), reveal measurable but by far not great differences in activation energies which range, disregarding the results of CaF_2, from 0.41 eV to 0.50 eV. These values are in good agreement with results from recently performed molecular dynamics studies.[27] For nanocrystalline CaF_2 background effects are predominant

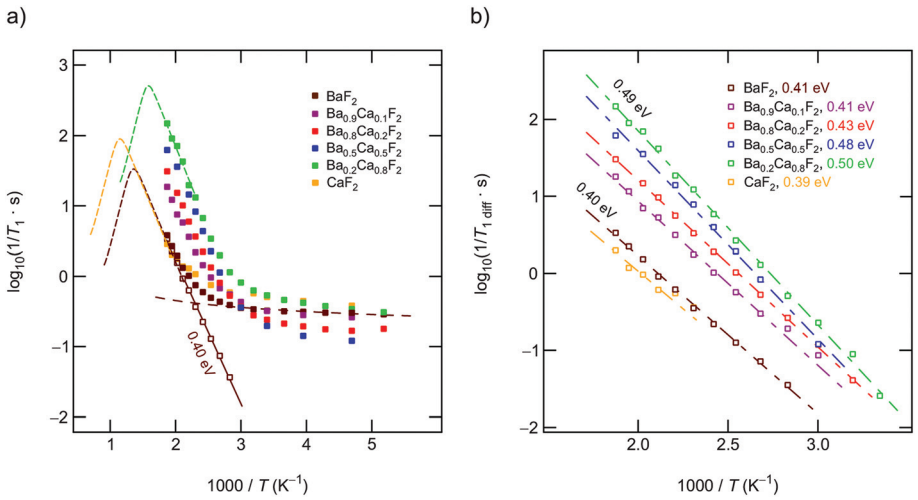

Fig. 4 (a) Temperature dependence of the ^{19}F NMR SLR rates $1/T_1$ (282.0 MHz). A power law is used to extrapolate the background rates to higher T to obtain purely diffusion-induced relaxation rates $1/T_{1\mathrm{diff}}$. The dashed lines indicate possible positions of the peak maxima. (b) Diffusion induced ^{19}F NMR rates after the correction procedure. The lines show linear fits to extract NMR activation energies, which range from 0.40 to 0.49 eV.

in the T range investigated; these effects do not allow the proper determination of an activation energy in the T range covered. Here, we estimated E_a after background correction to be approximately 0.39 eV. The better the flank is accessible the more precise the activation energy can be determined.

Fig. 4(b) entails two important information. First, the absolute rates $1/T_{1\mathrm{diff}}$ increase with increasing x and sharply decrease if x exceeds 0.8. As a function of x, the diffusion-induced rates pass through a maximum that is similar, but not exactly the same, to that seen *via* DC conductivity spectroscopy. T_1 is most effective for Ca-rich samples, see the rates for x = 0.8. Apart from this small but important distinctions, the rates support the mixed earthy-alkaline effect observed in our earlier study.[28] Second, the activation energies from NMR turn out to be smaller than those seen by DC conductivity spectroscopy (see Table 1). Furthermore, their overall change with composition is less pronounced as seen for long-range ion transport.[28] In contrast to conductivity measurements, E_a from NMR pass through a very shallow maximum (*ca.* 0.5 eV at x = 0.5) rather than a minimum.

To further support the activation energies obtained according the correction procedure sketched above, we also analyzed our T_1 data with an Arrhenius fit that directly takes into account the deviation at low temperatures with the help of a power law ansatz: $1/T_1 = c\cdot\exp(-E_a/(k_BT)) + a\cdot(1/T)^n$. c and a denote fitting parameters. The exponent n ($0.4 < n < 1.2$) should agree with β. It characterizes the type of relaxation, *e.g.*, driven by coupling of the spins to electrons or phonons, being

Table 1 Activation energies and ionic conductivities as derived from conductivity and NMR spectroscopy for the samples milled for 10 h in a high-energy planetary mill. Note that E_a from NMR, as well as E'_a, steadily increases from x = 0 to x = 0.8 although σ_{DC} and $E_a(\sigma_{DC})$ pass through a maximum and a minimum, respectively

	Conductivity spectroscopy			NMR relaxation				
x	E_a	σ_{DC} (298 K) (S cm^{-1})	$\log(\sigma_0$/S cm^{-1} K)	E_a (T_1)[a] (eV)	$E'_a(T_1)$[f] (eV)	E_a ($T_{1\rho}$) (eV)	α[g]	
0	0.78	1.6×10^{-11}	5.17	0.41	0.43	0.19	1.51	Low-T flank not completely reached
0.1	—	—	—	0.41	0.45	0.17		
0.2	0.64[b]	4.6×10^{-9}	5.06	0.43	0.43	0.22	1.66	
0.5	0.61[c]	1.6×10^{-8}	5.23[e]	0.49	0.46	0.29	1.80	$E_a(T_1)$ = 0.35 eV,[a,h] for t_{mill} = 100 h.
0.8	0.71[d]	8.7×10^{-10}	5.52	0.50	0.51	0.32	1.70	
1.0	0.80	7.2×10^{-14}	3.41	0.39	0.35	0.09	1.39	Low-T flank only partly accessible below 500 K

[a] Corrected values that take into account a non-diffusive background; the error for all values is ±0.01 eV. [b] Activation energy read off at 1 MHz: 0.50 eV. [c] 0.58 eV (1 MHz). [d] 0.55 eV (1 MHz). [e] After 100 h of milling a value of 5.44 is obtained; the largest increase for the pre-factor is seen when comparing nanocrystalline CaF_2 with nanocrystalline BaF_2. [f] E'_a denotes values corrected using a joint fit of both diffusion and non-diffusive effects. [g] Values refer to $E_a(T_1)$; α = 2 would result for 3D (isotropic) uncorrelated motion. [h] For x = 0.5 and t_{mill} = 100 h we obtained E'_a = E_a = 0.35 eV. After 100 h of milling we obtain α = 1.54.

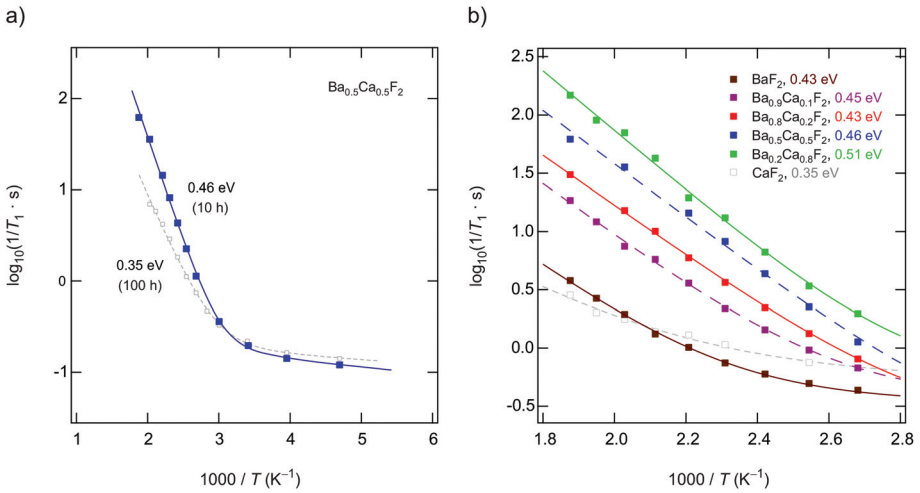

Fig. 5 (a) Temperature dependence of the ^{19}F NMR SLR rates $1/T_1$ (282.0 MHz) for nanocrystalline $Ba_{0.5}Ca_{0.5}F_2$ obtained after t_{mill} = 10 h and t_{mill} = 100 h. A joint fit of both diffusion and non-diffusive effects is used to obtain the activation energies. (b) Change of the low-T ^{19}F NMR $1/T_1$ rates of $Ba_{1-x}Ca_xF_2$ as a function of x. Solid and dashed lines show fits with the joint fit mentioned. The extracted NMR activation energies range from 0.35 to 0.51 eV.

responsible for the change in $1/T_1$ at low T. The fitting results are shown in Fig. 5; the activation energies E'_a are listed also in Table 1. E'_a is, for all samples, closely comparable with E_a.

Comparison with results from conductivity spectroscopy and ^{19}F NMR line shapes

To characterize long-range F ion transport through impedance spectroscopy, in Fig. 6(a) the conductivity isotherms of $Ba_{0.5}Ca_{0.5}F_2$ are shown. While at low frequencies and sufficiently high T electrode polarization effects show up, the main parts of the spectra are dominated by the so-called DC plateau ($\nu \rightarrow 0$) from which σ_{DC} can be read off. Pronounced dispersion regions are only visible at sufficiently low T. The DC plateau transforms into a semi-circle when the Nyquist representation is used to analyze the impedance data. The semi-circle shown in Fig. 6(b) is characterized by a capacity C of 3 pF which unequivocally points to a bulk electrical relaxation process. Blocking grain boundary resistances seem to be negligible. A value of 3 pF is also in perfect agreement with permittivities well below 10^2, see Fig. 6(c). The modulus representation, $M''(\nu)$, reveals single peaks with a width (full width at half maximum) larger than that expected for a Debye process,

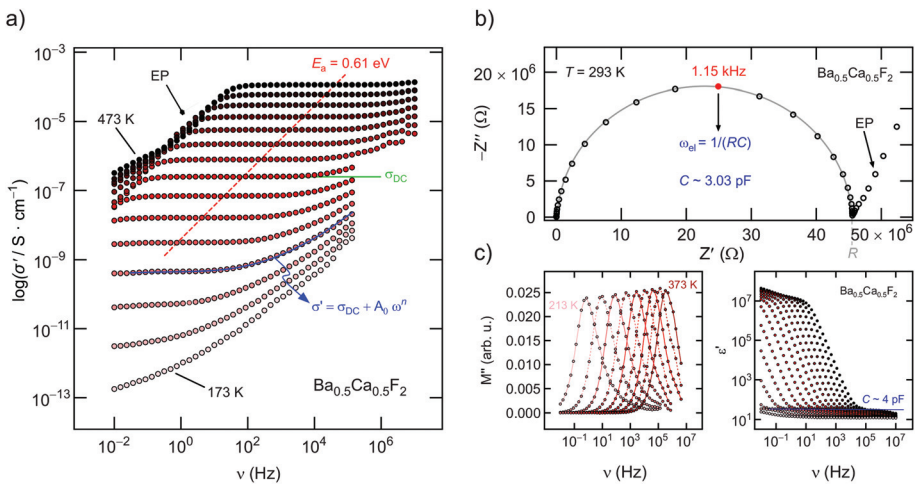

Fig. 6 (a) Conductivity isotherms of nanocrystalline $Ba_{0.5}Ca_{0.5}F_2$. A Jonscher-type power law is used to parameterize the dependency on frequency. While electrode polarization (EP) shows up at high T and low frequencies, at low T dispersive regions dominate the spectra. DC conductivities were read off from the frequency independent plateau regions. (b) Complex plane plot of the conductivity isotherm recorded at 293 K. Only one depressed semicircle is seen which corresponds to a relaxation process characterized by a capacity expected for a bulk response. The electrical relaxation frequency ω_{el} at 293 K is 1.15 kHz. (c) Modulus spectra and change of the real part of the complex permittivity with frequency in a temperature range between 173 K and 473 K (spectra recorded in steps of 20 K).

cf. Fig. 6(c). Hence, the F ions are subjected to correlated motion in $Ba_{0.5}Ca_{0.5}F_2$ sensing a distribution of diffusion pathways in an irregularly shaped potential landscape. Such dynamics are usually described with non-exponential motional correlation functions.[42]

Evaluating $\sigma_{DC}T$, see Fig. 7(a), illustrates that, depending on x, the activation energy for long-range ion transport varies from 0.80 eV (CaF_2, ball milled for 10 h) to 0.61 eV ($Ba_{0.5}Ca_{0.5}F_2$). Pure nanocrystalline BaF_2 (10 h) has to be characterized by 0.78 eV. These values perfectly agree with those published earlier.[28] In Fig. 7(b) we show the increase of $\sigma_{DC}T$ for $Ba_{0.5}Ca_{0.5}F_2$ with increasing milling time. While for a mixture of BaF_2 and CaF_2 milled for only 5 min σ_{DC} is still affected by the low-conducting CaF_2, milling for 1 h already results in a significant increase of the DC ionic conductivity exceeding that of nanocrystalline BaF_2 (10 h) by one order of magnitude. After 10 h of mechanical treatment the upper limit of σ_{DC} is reached. Further increase of t_{mill} does not change σ_{DC} significantly.

While for σ_{DC} the activation energy and the σ_0 in $\sigma_{DC}T = \sigma_0 \exp(-E_{a,\ DC}/k_BT)$ may vary with x, in ^{19}F NMR relaxometry the change of the NMR pre-factor $1/\tau_{0,\ NMR}$ (see below) seems to play a more significant role. This idea is illustrated in Fig. 4(a). The higher F anion conductivity in mixed samples is a proven fact. Indeed, ^{19}F NMR line shape measurements also show enhanced F anion hopping in the mixed samples as compared to the pure end members. In contrast to BaF_2 and CaF_2 the corresponding NMR lines of the samples with $0.2 < x < 0.8$ are composed of a clearly visible motionally narrowed contribution that is attributed to F anions being fast enough to average (homonuclear) dipole–dipole couplings (Fig. 8). As the rigid lattice ^{19}F NMR line width of BaF_2 (and CaF_2) is at least 30 kHz, full narrowing, which is already seen slightly above 400 K, corresponds to F jump rates $1/\tau_{NMR}$ in the order of 10^6 s^{-1}, see also the estimation below *via* spin-lock NMR. Such a value will definitely affect the low-T regime of SLR NMR. The peak maximum of the $1/T_1$ rate would be expected to show up if $1/\tau_{NMR}$ reaches values in the order of 1.8×10^9 s^{-1}.

As the rates of $Ba_{0.5}Ca_{0.5}F_2$ reveal the onset of the diffusion-induced low-T flank at lower temperatures we expect the corresponding rate peak, see dashed lines in Fig. 4(a), to show up at lower T as compared to BaF_2 and CaF_2, respectively. With the low-T activation energies being rather similar, especially if we consider the flanks of the samples with $x = 0.2$, $x = 0.5$ and $x = 0.8$, the only parameter that can further increase $1/\tau_{NMR}$ is the pre-factor in $1/\tau_{NMR} = 1/\tau_{0,\ NMR} \exp(-E_{a,\ high\text{-}T}/k_BT)$. Here, $E_{a,\ high\text{-}T}$ denotes the activation energy of the high-T flank of the peaks indicated in Fig. 5(a). The flank is inaccessible as the nanocrystalline samples are sensitive to grain growth and decomposition if NMR experiments were performed at too high temperatures. $E_{a,\ high\text{-}T}$ can be identified with $E_{a,\ DC}$. Although $E_{a,\ DC}$ change from 0.61 eV to 0.71 eV for x ranging from 0.2 to 0.8 (*cf.* Table 1), the variation in $E_{a,\ DC}$ alone could not explain the significant shift of the low-T flank. As for σ_0, also $1/\tau_0$ is, besides other factors, affected mainly by the attempt frequency ν_0, the activation entropy ΔS as well as the number of spins effectively taking part in ^{19}F NMR spin–lattice relaxation. The latter number is strongly associated to the concentration of available sites where the mobile ions can jump to. As has been shown recently, the softness of a lattice may influence ν_0.[43] In the present case, besides such an influence, effects of migration entropy, affected by both vibrational or configurational contributions, is expected to control the pre-factor mostly. Frenkel defects show a considerable high migration entropy that may especially affect the samples with $x = 0.5$ and $x = 0.8$.

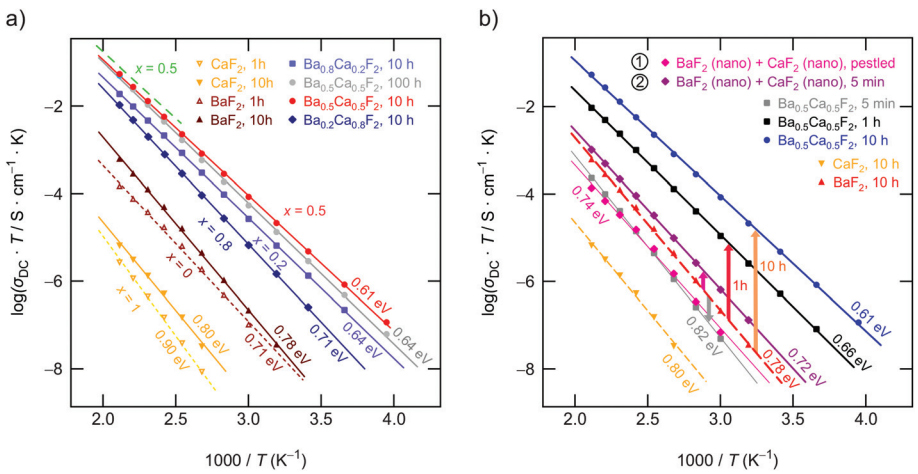

Fig. 7 (a) Change of the DC conductivity of $Ba_{1-x}Ca_xF_2$ as a function of inverse temperature. The highest conductivities are found for $x = 0.5$. While the solid lines show linear fits to extract activation energies for samples prepared by milling for $t_{mill} = 10$ h, dashed lines refer to samples milled for 1 h only. (b) Conductivity of $Ba_{0.5}Ca_{0.5}F_2$ samples prepared by high-energy ball milling and comparison to $BaF_2 : CaF_2$ mixtures, see text for further details. Samples 1 and 2 refer to compounds which have been prepared by mixing nanocrystalline BaF_2 ($t_{mill} = 10$ h) and CaF_2 ($t_{mill} = 10$ h) either by hand with mortar and pestle or by high-energy ball milling the two components for only 5 min. For the ball-milled sample even the 5 min milling procedure results in a measurable increase of $\sigma_{DC}T$.

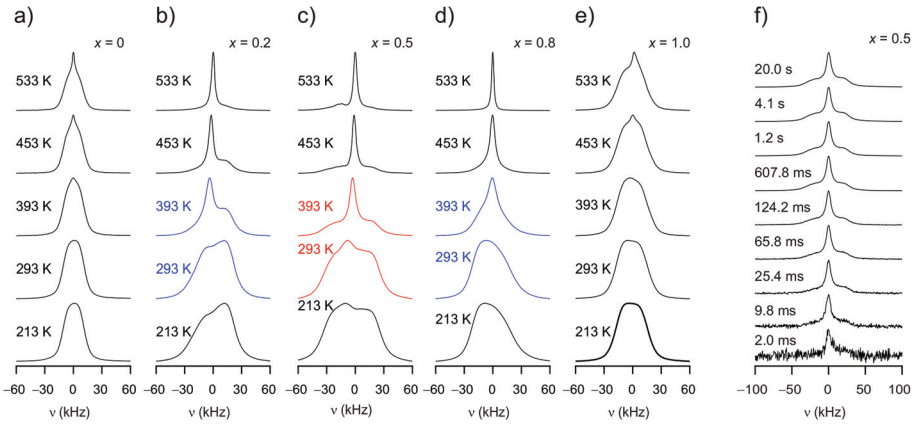

Fig. 8 (a) to (e) Variable-temperature ^{19}F NMR spectra of $Ba_{1-x}Ca_xF_2$ (282.0 MHz, static conditions). At low T broad NMR lines are seen. Broadening is due to dipole–dipole couplings and the existence of a (partially) mixed F environments with distinct chemical shifts. Spectra are shown such that the centre of the NMR signal is located at 0 kHz. As T increases heterogeneous motional narrowing sets in. The narrowed line, which emerges with increasing temperature at the centre of the NMR signal, reflects the number fraction of mobile F anions with respect to the NMR time scale. For x = 0.5 and T = 393 K the area fraction of this NMR line is larger for x = 0.5 than for x = 0.2 and x = 0.8. (f) Evolution of the ^{19}F NMR Fourier transforms in the frame of a T_1 saturation recovery experiment, that is, spectra obtained at different waiting times t. Strong spin-diffusion effects account for a single spin temperature with no differences in T_1 relaxation for both the narrow and the broad NMR spectral components.

As can be clearly inferred from the ^{19}F NMR spectra (Fig. 8(a)–(e)), the number fraction of mobile F anions, which are represented by the motionally narrowed lines for each sample, passes through a maximum at x = 0.5. This is best seen at T = 393 K. For the sake of clarity we deconvoluted the spectra with appropriate Voigt functions to estimate the area fraction A_f of the motionally narrowed NMR component (see Fig. 9).[12] The larger the number of mobile ions, performing net displacements as well as local jumps, the more effective spin fluctuations. Of course, the x-dependent number of effective charge carriers will, to some extent, also affect σ_0, which is related to long-range ion transport. It turned out, however, that its influence on localized jump processes is much larger.

Although F anion dynamics is clearly heterogeneous in $Ba_{x-1}Ca_xF_2$, effective spin-diffusion, *i.e.*, flip-flop processes without any mass transfer, ensures homogeneous relaxation of the spin system. Accordingly, the ^{19}F NMR transients do not feature a two-step decay of fast and slowly relaxing components as it has been seen for other nanocrystalline core–shell model systems.[32–34] In the frame of a saturation recovery experiment ^{19}F NMR spectra uniformly buildup with increasing waiting time (see Fig. 8(f)). Thus, there is fast communication between all ^{19}F spins in mixed $Ba_{0.5}Ca_{0.5}F_2$.

Influence of correlated motion on activation energies

Understanding the slight increase in $E_{a,\ low\text{-}T}$ when going from x = 0.2 (0.43 eV) to x = 0.5 (0.48 eV) and further to x = 0.8 (0.50 eV) also needs our attention. Although perhaps not applicable to our disordered system with relatively low barriers, the trend of both pre-factor and E_a from NMR resembles that of the Meyer–Neldel rule after which a higher activation energy is associated with a higher pre-factor.[44] In our case, however, we have to consider the following. In contrast to $E_{a,\ high\text{-}T}$, $E_{a,\ low\text{-}T}$

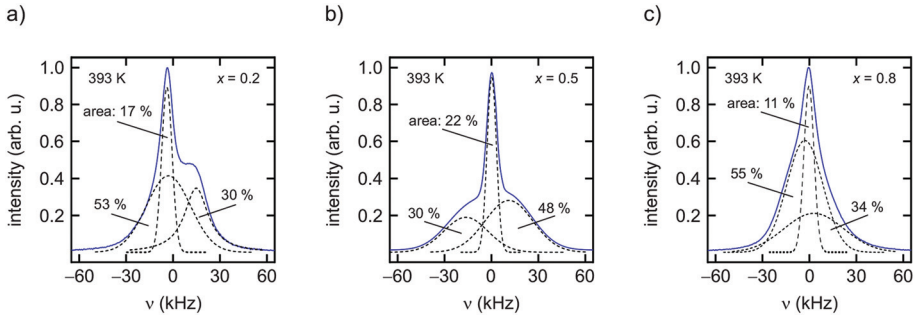

Fig. 9 (a) to (c) ^{19}F NMR spectra of $Ba_{1-x}Ca_xF_2$ (x = 0.2, x = 0.5 and x = 0.8) recorded at 393 K (282.0 MHz). In order to estimate the area fraction of the narrow component several Gaussian curves were used to deconvolute the spectra. The narrowed lines at the centre of the NMR signals reflect the number fraction A_f of mobile F anions. For x = 0.5 approximately 20% participate in fast ion dynamics. Although the Ca-rich sample with x = 0.8, see also the corresponding XRD pattern, is characterised by A_f of only 11%, ^{19}F relaxation is most effective for this sample. The mixed but Ca-rich regions seem to facilitate nuclear spin relaxation.

is a so-called apparent activation energy that is additionally affected by correlation effects.[45] It is comparable to AC conductivity activation energies read off in the dispersive regions of the conductivity isotherms (see also Table 1).[16] The larger the impact of correlation effects, such as structural disorder and Coulomb interactions of F^- interstitials and vacancies, the larger the difference between $E_{a,\ high\text{-}T}$ and $E_{a,\ low\text{-}T}$. The two activation energies are linked according to the following relation $E_{a,\ low\text{-}T} = (\alpha - 1)E_{a,\ high\text{-}T}$.[46] For 3D uncorrelated motion the parameter α equals 2. Correlated motion results in $\alpha < 2$ and, thus, yields asymmetric NMR rate peaks.[45] Here it turned out that α pass through a maximum located near $x = 0.5$ (see Table 1). This result means less correlated motion for the samples with the highest diffusion-induced relaxation rates. To be clear, in all samples correlated motion is sensed by NMR; its extent, however, seems to be less for local ion dynamics in samples milled just for 10 h and $x = 0.5$ or $x = 0.8$. It is evident from XRPD and ^{19}F MAS NMR that under these conditions mixing at atomic scale is incomplete; ^{19}F MAS NMR revealed that the same is true for the sample with $x = 0.8$. Therefore, fast F anion diffusion might occur along or near Ca- and Ba-rich regions as mentioned above. Precisely speaking, diffusion induced T_1 relaxation is more effective for $x = 0.8$, *i.e.*, for mixed but Ca-rich environments.

.Recently, we probed a very similar trend of α for Li ion diffusivity in layer-structured 2H-Li_yNbS_2.[47] Although in 2H-Li_yNbS_2 Li diffusivity decreases when y approaches $y = 1$, which is the maximum Li load, the low-T activation energy in deduced from $T_1(T)$ measurements steadily decreases when going from $y = 0.3$ to $y = 1.0$. This effect has been ascribed to an increasing effect of correlated ion motion which is maximal when the van-der-Waals gap in NbS_2 is completely filled with Li ions. At the same time, also dipolar magnetic and electric quadrupolar interactions increase the larger the Li concentration.

Here, the origin of correlated motion in mixed $Ba_{x-1}Ca_xF_2$ is, however, definitely different from that seen for 2H-Li_yNbS_2. An increasing number fraction of mobile F spins, activation entropy contributions and lower long-range activation energies cause a sharp increase in Li diffusivity and ionic conductivity when mixed phases are formed. For all samples correlated motion is expected because the ions are subjected to a highly irregular potential landscape, including also metastable states. The extent and origins of correlation effects seem, however, change with composition. According to the NMR factor α the Ba-rich phases ($x = 0.1$, $x = 0.2$) provide an additional source of correlated motion leading to lower apparent activation energies than expected. Zahn *et al.* pointed out differences in the concentration of mobile charge carriers when Ca or Ba ions are introduced in BaF_2 and CaF_2, respectively. At very low levels of doping, the incorporation of Ca^{2+} ions resulted in trapped F interstitial sites and mobile F vacancies as the opponent defect.[26] The formation of such interstitial site next to a Ca^{2+} dopant in BaF_2 was promoted by 0.08 eV. On the other hand, the generation of Frenkel defects in Ba-doped CaF_2 is energetically disfavored by 0.14 eV.[26]

In our case substitutional disorder is much larger than dopant concentrations and a direct comparison with results for extremely low levels of doping turns out to be difficult. At least we can say the following. Even if we consider complete and uniform mixing at atomic scale, we deal with samples that naturally have larger regions being rich in Ba^{2+}. Segregation effects in interfacial regions or clustering on the nm scale will lead to even larger non-uniform areas. As has been shown recently for several types of ion conductors, concerted ion movements always cause the mean activation barrier to decrease.[48] Thus, concerted and, thus, highly correlated ion movements in the vicinity of Ca-doped Ba-rich regions or at the interface of Ba-rich and Ca-rich regions in non-intimately mixed samples could serve as an explanation for the unusual ^{19}F NMR SLR behavior and the origin of additional correlation effects seen for the Ba-rich samples.

Obviously, on the angstrom length scale, to which ^{19}F SLR NMR is sensitive, this effect levels off when the region $0.5 \leq x \leq 0.8$ is reached. Note that also the activation energy of $Ba_{0.5}Ca_{0.5}F_2$ (0.58 eV, see Table 1), when determined from AC impedance spectroscopy at 1 MHz, is higher than that of $Ba_{0.2}Ca_{0.8}F_2$ (0.55 eV) and $Ba_{0.8}Ca_{0.2}F_2$ (0.50 eV). In this compositional range, the increase in mobile spins near non-uniformly mixed interfaces is more significant and leads to a further increase in diffusivity. Simultaneously, the impact of correlation effects on the low-T ^{19}F NMR T_1 measurements decreases, at least for samples milled for 10 h.

^{19}F NMR spin-lock NMR and the effect of long-term milling

If we consider the corresponding rates measured in the kHz range through spin-lock NMR, see Fig. 10(a) and (b), the activation energies seem to reflect the same behavior. Regarding the absolute values for E_a suggests, however, that the temperature dependence of the ^{19}F NMR SLR rates, see data for $x = 0.1$ and $x = 0.2$, are additionally influenced by other effects. Besides changes in the diffusion mechanisms, non-diffusive effects, such as spin-diffusion, presumably play the most important role. The characteristic spin-diffusion correlation times are expected to take values in the s to ms range, which fall into the time window of spin-lock NMR. Dipolarly coupled ^{19}F spins with short distances to each other are prone to be affected by flip-flop effects. Hence, $1/T_{1\rho}$ NMR rates are expected to be much larger influenced by spin-diffusion as laboratory-frame SLR measurements performed in the MHz to GHz range. Apart from such interfering effects, spin-lock NMR relaxation is most effective for the sample with $x = 0.5$. This finding mirrors the change of long-range ion dynamics as seen by DC conductivity measurements.

Up to here, we discussed results from samples prepared by milling the starting materials for 10 h. Except for $Ba_{0.5}Ca_{0.5}F_2$ our results from XRPD do not reveal any substantial amounts of the nanocrystalline binary parents. Increasing t_{mill} up to 100 h forces the earth alkaline ions to mix almost completely, as is also verified by ^{19}F MAS NMR. Importantly, the $1/T_{1\rho}$ rates, as well as the DC conductivity values, do not change when t_{mill} is increased from 10 to 100 h. Hence, bulk long-

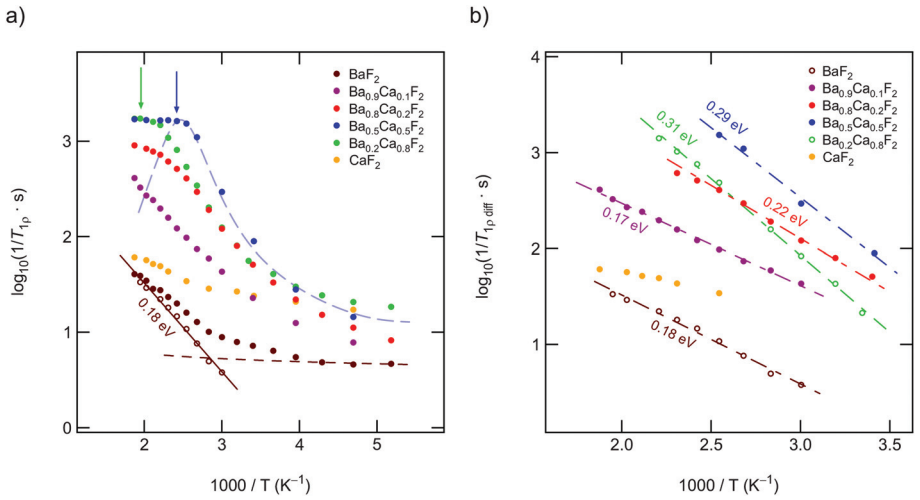

Fig. 10 (a) Arrhenius representation of the spin-lock ^{19}F MAS NMR rates $1/T_{1\rho}$ (100 kHz, 282.0 MHz) for $Ba_{1-x}Ca_xF_2$. As for T_1, we used a power law ansatz to correct the measured rates for any non-diffusive background relaxation, as indicated for the data referring to nanocrystalline BaF_2. The dashed line drawn through the data points of the $Ba_{0.5}Ca_{0.5}F_2$ sample is to guide the eye. The peak is located at the lowest possible temperature. For x = 0.2 and x = 0.8 we see that the peaks shift toward higher T (see vertical arrows). These shifts fully agree with a lower F anion diffusivity and, consequently, a lower F ion conductivity as seen through conductivity spectroscopy. (b) Diffusion induced ^{19}F NMR SLR rates $1/T_{1\rho\ \mathrm{diff}}$ rates after background correction.

range ion transport and spin-diffusion effects are already fully developed at shorter periods of mechanical treatment. In contrast, ^{19}F NMR spectra and $1/T_1$ do depend on t_{mill}. Although static line shapes reveal an increase of the number of mobile spins on the NMR time scale, this change does not cause an increase of σ_{DC}, see above (Table 1 and Fig. 7(a)). While the onset of the low-T ^{19}F NMR $1/T_1$ flank remains unchanged (see Fig. 4(b)), the corresponding activation energy decreases from E_a = 0.49 eV to only 0.35 eV. We attribute this unusual change in $E_a(T_1)$ to enhanced localized ion jump processes. Localized or caged jumps, including unsuccessful highly correlated forward–backward processes, will definitely affect the low-T $1/T_{1\mathrm{diff}}$ rates but do not contribute to net charge transport, which is sensed by σ' in the limit of low frequencies. This is the classical way to interpret differences between diffusion parameters derived from NMR and those from conductivity spectroscopy. In general, the two methods are sensitive to quite different kinds of motional (auto-)correlation functions, see above. The relationship between parameters from NMR and conductivity spectroscopy in disordered media, such as glasses, has been discussed in detail by Ngai and co-workers.[49–54]

Careful inspection of Fig. 7(a) shows that the sample milled for 100 h shows even lower conductivities as compared to that milled for 10 h. We also see a slight increase of the corresponding activation energy E_a (0.64 eV *vs.* 0.61 eV). This finding supports our idea that long-time milling, *i.e.*, the formation of solid-solution like environments, mainly lead to an increase of localized correlated motional processes. The corresponding factor α turned out to be 1.54. This value is lower than $\alpha \approx 1.8$ found for $Ba_{0.5}Ca_{0.5}F_2$, which was prepared using t_{mill} = 10 h. On the other hand, it resembles the behavior of nanocrystalline BaF_2. Obviously, the most favorable configurations for long-range ion transport are internal, heterogeneously intermixed interfaces between Ca-rich and Ba-rich regions, as discussed above. Complete mixing, or the formation of clusters with, *e.g.*, diameters of 1 nm, as suggested recently,[26] seems to be not needed to ensure effective long-range ion transport. Here, we assume that these heterogeneous regions act as non-stopping or percolating pathways similar to those in dispersed ion conductors.[32,33,55–58] Interestingly, these regions, acting as hosts for fast F anion diffusivity, have partly been formed already at shorter milling times of t_{mill} = 1 h (see Fig. 7(b)). As compared to nanocrystalline BaF_2 we see a considerable increase in σ_{DC} for such a sample. Even if we mix nanocrystalline BaF_2 and CaF_2, each separately milled for 10 h, for just 5 min in a planetary mill, we found a measurable increase in ionic conductivity. For these samples ^{19}F MAS NMR also points to a very low, but detectable fraction of F anions residing in or near the earth-alkaline mixed environments.

Self-diffusion coefficient

In contrast to the T_1 measurements, the spin-lock data (see Fig. 10(a)) reveal the beginning of a peak maximum from which we can finally deduce an upper limit of a diffusion coefficient. Interestingly, at the temperature where $1/T_{1\rho}$ passes through a maximum, in many cases the corresponding stretching factor, κ, takes its minimal value (see Fig. 3(c)). At the $1/T_{1\rho}$ peak maximum the F anion jump rate τ_{NMR} should be in the order of the (effective) locking frequency. Using $\omega_1/2\pi$ = 100 kHz as a lower limit, *via* $\omega_1\tau = 0.5$ we estimate $1/\tau_{\mathrm{NMR}}$ to be in the order of 1.3×10^6 s^{-1} at 410 K (x = 0.5). This value translates into a self-diffusion coefficient of $D_{410\ \mathrm{K}} = a^2/(6\tau_{\mathrm{NMR}})$ of 1.8×10^{-14} m^2 s^{-1}. Here, a denotes the average jump distance;

for $Ba_{0.5}Ca_{0.5}F_2$ we used a = 2.92 Å as a good approximation of the mean F–F distance in $Ba_{0.5}Ca_{0.5}F_2$ (10 h). $D_{410\ K}$ is a typical value for a moderate ionic conductor. The diffusion coefficient determined at the rate maximum of a spin-lock experiment carried out at 100 kHz should be comparable to that which we obtain when DC conductivities are analyzed that probe successful ion displacements. With the ionic conductivity at 410 K we estimated a solid-state diffusion coefficient *via* the Nernst–Einstein relation, $D_\sigma = \sigma_{DC} k_B T/(q^2 N)$ with q being the charge of the F anions and N the number density of charge carriers. From ^{19}F NMR we know that approximately 20% of the ions take part in ionic conduction. In this case $D_{\sigma,\ 410\ K}$ amounts to 1.7×10^{-14} m^2 s^{-1}, which is very close to the Einstein–Smoluchowski diffusion coefficient. For x = 0.8 the corresponding $1/T_{1\rho}$ peak is shifted toward higher T, directly reflecting the decrease in σ_{DC} as seen in Fig. 7(a). For x = 0.2, *i.e.*, Ba-rich samples, strongly correlated motions (see above) and spin-diffusion effects govern the low-T ^{19}F NMR spin-lock rates.

Summary and conclusions

Mechanical treatment of CaF_2 and BaF_2 in high-energy ball mills leads to the formation of metastable $Ba_{x-1}Ca_xF_2$. Long-range ion transport is maximized for equimolar compositions and E_a, determined from DC conductivity measurements, passes through a minimum value (0.61 eV) at this composition. Through ^{19}F NMR relaxometry measurements, being in our case sensitive to short-range F anion dynamics, we tried to sharpen this picture. Here, we showed that ion dynamics on the angstrom length scale is characterized by very similar activation energies if x varies from 0.2 (0.43 eV) to 0.5 (0.50 eV). The increase of the absolute ^{19}F SLR NMR rates can be explained by an increase of the pre-factor of the underlying Arrhenius equation, which is, besides other factors, governed by the activation entropy. For all samples we observed highly correlated ionic motion. While macroscopic properties, such as σ_{DC}, do not depend much on milling time; short-range order and motional correlation effects do. By comparing the various samples prepared we conclude that F anion diffusivity in earth-alkaline mixed interfacial regions, either rich in Ba or Ca, mainly boost long-range ion transport. Extensive mixing of the cations during long milling periods, on the other hand, primarily influences short-range ion dynamics.

Conflicts of interest

There are no conflicts to declare.

Acknowledgements

We thank Veronika Pregartner for her help with sample preparation and characterization. Financial support by the Deutsche Forschungsgemeinschaft (DFG Research Unit 1277, grant no. WI3600/2-1(4-1) and WI3600/5-2 (SPP 1415)) as well as by the Austrian Federal Ministry of Science, Research and Economy, and the Austrian National Foundation for Research, Technology and Development (Christian Doppler Laboratory of Lithium Batteries: Ageing Effects, Technology and New Materials) is greatly appreciated.

References

1 P. G. Bruce, B. Scrosati and J. M. Tarascon, *Angew. Chem., Int. Ed.*, 2008, **47**, 2930–2946.
2 B. Dunn, H. Kamath and J. M. Tarascon, *Science*, 2011, **334**, 928–935.
3 J. B. Goodenough and K. S. S. Park, *J. Am. Chem. Soc.*, 2013, **135**, 1167–1176.
4 J. C. Bachman, S. Muy, A. Grimaud, H. H. Chang, N. Pour, S. F. Lux, O. Paschos, F. Maglia, S. Lupart, P. Lamp, L. Giordano and Y. Shao-Horn, *Chem. Rev.*, 2016, **116**, 140–162.
5 A. S. Arico, P. Bruce, B. Scrosati, J. M. Tarascon and W. Van Schalkwijk, *Nat. Mater.*, 2005, **4**, 366–377.
6 M. Anji Reddy and M. Fichtner, *J. Mater. Chem.*, 2011, **21**, 17059–17062.
7 P. Heitjans and S. Indris, *J. Phys.: Condens. Matter*, 2003, **15**, R1257–R1289.
8 A. Chadwick and S. Savin, *Solid State Ionics*, 2006, **177**, 3001–3008.
9 J. Maier, *Chem. Mater.*, 2014, **26**, 348–360.
10 J. Maier, *Phys. Chem. Chem. Phys.*, 2009, **11**, 3011–3022.
11 J. Maier, *Z. Phys. Chem.*, 2003, **217**, 415–436.
12 P. Heitjans, M. Masoud, A. Feldhoff and M. Wilkening, *Faraday Discuss.*, 2007, **134**, 67–82.
13 F. Preishuber-Pflügl, V. Epp, S. Nakhal, M. Lerch and M. Wilkening, *Phys. Status Solidi C*, 2015, **12**, 10–14.
14 D. Wohlmuth, V. Epp, P. Bottke, I. Hanzu, B. Bitschnau, I. Letofsky-Papst, M. Kriechbaum, H. Amenitsch, F. Hofer and M. Wilkening, *J. Mater. Chem. A*, 2014, **2**, 20295–20306.
15 V. Epp and M. Wilkening, *ChemPhysChem*, 2013, **14**, 3706–3713.
16 M. Wilkening, V. Epp, A. Feldhoff and P. Heitjans, *J. Phys. Chem. C*, 2008, **112**, 9291–9300.
17 F. Preishuber-Pflügl, P. Bottke, V. Pregartner, B. Bitschnau and M. Wilkening, *Phys. Chem. Chem. Phys.*, 2014, **16**, 9580–9590.
18 V. Epp and M. Wilkening, in *Handbook of Solid State Batteries*, World Scientific, Singapore, 2015, ch. Li dynamics in solids as seen via NMR relaxometry.
19 M. Heise, G. Scholz, A. Düvel, P. Heitjans and E. Kemnitz, *Solid State Sci.*, 2016, **60**, 65–74.
20 G. Scholz, S. Breitfeld, T. Krahl, A. Düvel, P. Heitjans and E. Kemnitz, *Solid State Sci.*, 2015, **50**, 32–41.
21 H. Bhatia, D. T. Thieu, A. H. Pohl, V. S. K. Chakravadhanula, M. H. Fawey, C. Kubel and M. Fichtner, *ACS Appl. Mater. Interfaces*, 2017, **9**, 23707–23715.

22 C. Rongeat, M. A. Reddy, R. Witter and M. Fichtner, *ACS Appl. Mater. Interfaces*, 2014, **6**, 2103–2110.
23 C. Rongeat, M. A. Reddy, R. Witter and M. Fichtner, *J. Phys. Chem. C*, 2013, **117**, 4943–4950.
24 B. Ruprecht, M. Wilkening, A. Feldhoff, S. Steuernagel and P. Heitjans, *Phys. Chem. Chem. Phys.*, 2009, **11**, 3071–3081.
25 B. Ruprecht, M. Wilkening, S. Steuernagel and P. Heitjans, *J. Mater. Chem.*, 2008, **18**, 5412–5416.
26 D. Zahn, P. Heitjans and J. Maier, *Chem. – Eur. J.*, 2012, **18**, 6225–6229.
27 A. Düvel, P. Heitjans, P. Fedorov, G. Scholz, G. Cibin, A. V. Chadwick, D. M. Pickup, S. Ramos, L. W. L. Sayle, E. K. L. Sayle, T. X. T. Sayle and D. C. Sayle, *J. Am. Chem. Soc.*, 2017, **139**, 5842–5848.
28 A. Düvel, B. Ruprecht, P. Heitjans and M. Wilkening, *J. Phys. Chem. C*, 2011, **115**, 23784–23789.
29 N. Sata, K. Eberman, K. Eberl and J. Maier, *Nature*, 2000, **408**, 946–949.
30 J. Maier, *Prog. Solid State Chem.*, 1995, **23**, 171–263.
31 J. Maier, *J. Phys. Chem. Solids*, 1985, **46**, 309–320.
32 M. Wilkening, S. Indris and P. Heitjans, *Phys. Chem. Chem. Phys.*, 2003, **5**, 2225–2231.
33 S. Indris and P. Heitjans, *J. Non-Cryst. Solids*, 2002, **307**, 555–564.
34 P. Heitjans and M. Wilkening, *Mater. Res. Bull.*, 2009, **34**, 915–922.
35 D. C. Look and I. J. Lowe, *J. Chem. Phys.*, 1966, **44**, 2995–3000.
36 S. Indris, D. Bork and P. Heitjans, *J. Mater. Synth. Process.*, 2000, **8**, 245–250.
37 A. L. Patterson, *Phys. Rev.*, 1939, **56**, 978–982.
38 A. V. Chadwick, A. Düvel, P. Heitjans, D. M. Pickup, S. Ramos, D. C. Sayle and T. X. T. Sayle, *IOP Conf. Ser.: Mater. Sci. Eng.*, 2015, **80**, 012005.
39 D. Wohlmuth, V. Epp, B. Stanje, A. M. Welsch, H. Behrens and M. Wilkening, *J. Am. Ceram. Soc.*, 2016, **99**, 1687–1693.
40 M. Wilkening and P. Heitjans, *Phys. Rev. B: Condens. Matter Mater. Phys.*, 2008, **77**, 024311.
41 M. Wilkening, D. Bork, S. Indris and P. Heitjans, *Phys. Chem. Chem. Phys.*, 2002, **4**, 3246–3251.
42 B. Ruprecht, H. Billetter, U. Ruschewitz and M. Wilkening, *J. Phys.: Condens. Matter*, 2010, **22**, 245901.
43 M. A. Kraft, S. P. Culver, M. Calderon, F. Bocher, T. Krauskopf, A. Senyshyn, C. Dietrich, A. Zevalkink, J. Janek and W. G. Zeier, *J. Am. Chem. Soc.*, 2017, **139**, 10909–10918.
44 W. Meyer and H. Neldel, *Phys. Z.*, 1937, **38**, 1014–1019.
45 P. Heitjans, A. Schirmer and S. Indris, in *Diffusion in Condensed Matter – Methods, Materials, Models*, ed. P. Heitjans and J. Kärger, Springer, Berlin, 2005, pp. 367–415.
46 M. Uitz, V. Epp, P. Bottke and M. Wilkening, *J. Electroceram.*, 2017, **38**, 142.
47 B. Stanje, V. Epp, S. Nakhal, M. Lerch and M. Wilkening, *ACS Appl. Mater. Interfaces*, 2015, **7**, 4089–4099.
48 X. F. He, Y. Z. Zhu and Y. F. Mo, *Nat. Commun.*, 2017, **8**, 15893.
49 K. L. Ngai, *Solid State Ionics*, 1998, **105**, 225–230.
50 K. L. Ngai, *Phys. Rev. B: Condens. Matter Mater. Phys.*, 1993, **48**, 13481–13485.
51 V. Blache, J. Forster, H. Jain, O. Kanert, R. Kuchler and K. L. Ngai, *Solid State Ionics*, 1998, **113**, 723–731.
52 O. Kanert, R. Kuchler, K. L. Ngai and H. Jain, *Phys. Rev. B: Condens. Matter Mater. Phys.*, 1994, **49**, 76–82.
53 K. L. Ngai and O. Kanert, *Solid State Ionics*, 1992, **53**, 936–946.
54 O. Kanert, J. Steinert, H. Jain and K. L. Ngai, *J. Non-Cryst. Solids*, 1991, **131**, 1001–1010.
55 C. C. Liang, *J. Electrochem. Soc.*, 1973, **120**, 1289–1292.
56 S. Indris, P. Heitjans, M. Ulrich and A. Bunde, *Z. Phys. Chem.*, 2005, **219**, 89–103.
57 M. Ulrich, A. Bunde, S. Indris and P. Heitjans, *Phys. Chem. Chem. Phys.*, 2004, **6**, 3680–3683.
58 S. Indris, P. Heitjans, H. E. Roman and A. Bunde, *Phys. Rev. Lett.*, 2000, **84**, 2889–2892.